Journal of Molecular Structure 1254 (2022) 132280

Contents lists available at ScienceDirect

Journal of Molecular Structure

journal homepage: www.elsevier.com/locate/molstr

Crystal structure, Hirshfeld surface analysis, and molecular dynamics simulations of two isostructural N-propargyl-4-(2-oxopyrrolidin-1-yl)-1,2,3,4-tetrahydroquinolines

Fausto M. Güiza[a], Yeray A. Rodríguez-Núñez[b], David Ramírez[c,1], Arnold R. Romero Bohórquez[a], José Antonio Henao[d], Robert A. Toro[d], José Miguel Delgado[e], Graciela Díaz de Delgado[e,*]

[a] Grupo de Investigación en Compuestos Orgánicos de Interés Medicinal (CODEIM), Parque Tecnológico Guatiguará, Universidad Industrial de Santander, Piedecuesta, Colombia
[b] Departamento de Ciencias Químicas, Facultad de Ciencias Exactas, Universidad Andrés Bello, Quillota 980, 2531015 Viña del Mar, Chile
[c] Instituto de Ciencias Biomédicas, Facultad de Ciencias de la Salud, Universidad Autónoma de Chile, El Llano Subercaseaux 2801- Piso 5, 8900000 Santiago, Chile
[d] Grupo de Investigación en Química Estructural (GIQUE), Universidad Industrial de Santander, Bucaramanga, Colombia
[e] Laboratorio de Cristalografía – LNDRX, Universidad de los Andes, Mérida, Venezuela

ARTICLE INFO

Article history:
Received 8 October 2021
Revised 17 December 2021
Accepted 23 December 2021
Available online 28 December 2021

Keywords:
Cationic Povarov reaction
Tetrahydroquinoline
N-propargylamines
Crystal structure
Molecular dynamics simulations
Monoamine oxidase B inhibitors

ABSTRACT

Two new *N*-propargyl-4-(2-oxopyrrolidin-1-yl)-1,2,3,4-tetrahydroquinoline derivatives (**4a** and **4b**), have been efficiently prepared through a one-pot $InCl_3$-catalyzed cationic Povarov reaction between *N*-propargylanilines (**1a** and **1b**), formaldehyde (**2**) and *N*-vinyl-pyrrolidin-2-one (**3**). These compounds were characterized by ATR-FTIR spectroscopy, $^1H/^{13}C$ NMR spectroscopy, ESI-IT mass spectrometry, and by single-crystal X-ray diffraction. *N*-propargyl-6-methyl-4-(2′-oxopyrrolidin-1′-yl)-1,2,3,4-tetrahydroquinoline (**4a**) and *N*-propargyl-6-chloro-4-(2′-oxopyrrolidin-1′-yl)-1,2,3,4-tetrahydroquinoline (**4b**) are isostructural and crystallize in space group $P2_1/c$. The crystal structures are characterized by inversion-related interpenetrated helices along the *b*-axis that form columns along the *c*-axis. C—H···O, C—H···C, and C—H···π(aryl) for **4a** and C—H···O, C—H···Cl, and C—H···π(aryl) for **4b** interactions occur within the columns which are connected by C—H···π(propargyl) interactions. These features were further visualized by Hirshfeld surface analysis and energy frameworks calculations and evaluated by the E_{XY} enrichment ratio. Molecular dynamics simulations show that these compounds are promising monoamine oxidase B (MAO-B) inhibitors, since they interact with MAO-B in a similar manner as rasagiline, a drug commonly used in the treatment of Parkinson's and Alzheimer's diseases.

1. Introduction

The *N*-propargylamine scaffold continues to spark great interest in organic synthesis due to its use as a versatile precursor for obtaining heterocyclic compounds of a wide structural diversity. Thus, it is possible to use *N*-propargylamines to build pyrrole [1] and pyrazine [2] rings from aldehydes, pyridine rings from propinones, *N*-heteroarenes through cascade reaction [3], oxazolidinones, thiazolidines, and imidazoles from different heteroallenes [4–7], and coumarins from β-keto esters [8], among other heterocyclic nuclei of biological interest.

Besides being a versatile molecular building block, *N*-propargylamine compounds are important in the biological field due to their potential and direct pharmacological application. Derivatives of these compounds have been evaluated and reported as antioxidants [9], LSD1 inhibitors [10], antiarrhythmic agents [11], CYP2A6 inhibitors [12], and antitumor agents [13]. In addition, these compounds have commonly been reported as potential neuroprotective agents against diseases such as Parkinson's and Alzheimer's, because they contribute to the inhibition of the monoamine oxidase B (MAO-B) enzyme, one of the main therapeutic targets in the treatment of these illnesses [14–15].

* Corresponding author.
E-mail addresses: fausto.marin1@correo.uis.edu.co (F.M. Güiza), yenuro30@gmail.com (Y.A. Rodríguez-Núñez), david.ramirez@uautonoma.cl (D. Ramírez), arafrom@uis.edu.co (A.R. Romero Bohórquez), jahenao@uis.edu.co (J.A. Henao), toro.robert@gmail.com (R.A. Toro), jmdq2000@gmail.com (J.M. Delgado), gdiazdedelgado@gmail.com (G. Díaz de Delgado).
[1] Present address: Departamento de Farmacología, Facultad de Ciencias Biológicas, Universidad de Concepción, Concepción, Chile. email: dramirezs@udec.cl.

https://doi.org/10.1016/j.molstruc.2021.132280
0022-2860/

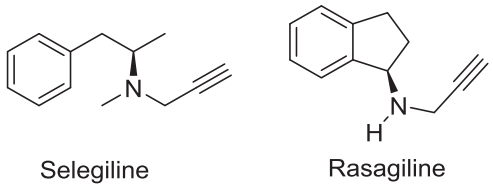

Fig. 1. *N*-propargyl amine drugs with high affinity and selectivity against MAO-B.

Selegiline and Rasagiline (Fig. 1) are two examples of irreversible drugs that carry the *N*-propargylamine scaffold and have high affinity and selectivity for MAO-B, leading to its inhibition [16]. These compounds form a covalent adduct with the flavin adenine dinucleotide co-factor (FAD) present in the active site of the enzyme [17]. Some published reports correlate the neuroprotective effect of these compounds with the presence of the *N*-propargyl group [14, 18].

Similarly, the *N*-propargyl fragment can link to other scaffolds of biological interest such as tetrahydroquinolines (THQ) and tetrahydroisoquinolines (TIQ) aiming at potentiating its activity. Some authors have reported *N*-propargyl TIQ compounds as neuroprotective and antiparkinson agents [19, 20]. We have previously synthesized several series of *N*-propargyl THQ compounds, which were tested as antioxidant agents [21] and as acetyl (AChE) and butyrylcholinesterase (BChE) inhibitors, critical therapeutic targets in the palliative treatment of Alzheimer's disease. Compounds **4a** and **4b** (Scheme 1) showed affinity on the active site of AChE and BChE and displayed a moderate inhibitory activity on these enzymes. The bioinformatic analysis carried out through docking and free energy calculations showed that the stability of the compounds in the active sites of these enzymes was mainly due to the aromatic fragment of THQ generating π-π stacking type interactions [22]. Based on the information above and keeping in mind the remarkable activity of *N*-propargylaniline derivatives as monoamine oxidase inhibitors, two members of this series of compounds, with different substituents on the C-6 position, were studied by single-crystal X-ray diffraction and are reported in this contribution. This study was complemented by Hirshfeld surface analysis, energy frameworks calculations, and contact enrichment ratios. In addition, we studied the possible interaction modes of these compounds compared to the drug rasagiline through Molecular Dynamics simulations (MDs). Finally, the FAD-ligand adducts were generated and subjected to MDs, demonstrating clear similarities in how these ligands interact with MAO-B.

With this work we want to emphasize that the crystallographic analysis together with the study of molecular dynamics constitute an important synergistic methodology to determine the favored contacts and the stability of the analyzed compounds in the active site of the MAO-B protein. This can help establish a criterion to assess the potential therapeutic use of these compounds. This protocol can be extended to other types of small molecules and proteins if their crystal structures are available.

2. Experimental section

2.1. Materials and methods

Chemical reagents were purchased from Merck, J.T. Baker, and Sigma-Aldrich, and used without further purification. The reaction progress was monitored using thin layer chromatography on PF254 TLC aluminum sheets from Merck. Column chromatography was performed using Silica gel (60-120 mesh). The melting points (uncorrected) were determined using a Fisher-Johns melting point apparatus. IR spectra were recorded on a FTIR Bruker Tensor 27 spectrophotometer coupled to a Bruker platinum ATR cell. Mass spectra were recorded on an ESI-IT Amazon X (Bruker Daltonics) with direct injection, operating in Full Scan mode at 300 °C and 4500 V in the capillary, using nitrogen as nebulizer gas with an influx of 8 L/min and 30 psi. Elemental analyses were performed on a Thermo Scientific CHNS-O analyzer (Model Flash 2000) and were within ± 0.4 of theoretical values. Nuclear magnetic resonance (NMR) spectra (^{1}H and ^{13}C) were measured on a Bruker Ultrashield-400 spectrometer (400 MHz ^{1}H NMR and 100 MHz ^{13}C NMR), using $CDCl_3$ as solvent and reference. *J* values are reported in Hz; chemical shifts are reported in ppm (δ) relative to the solvent peak (residual $CHCl_3$ in $CDCl_3$ at 7.26 ppm for protons). Signals were designated as follows: s, singlet; d, doublet; dd, doublet of doublets; ddd, doublet of doublets of doublets; t, triplet; td, triplet of doublets; q, quartet; m, multiplet; br, broad.

2.2. Synthesis of N-propargyl-4-(2-oxopyrrolidin-1-yl)-1,2,3,4-tetrahydroquinolines 4a and 4b

Compounds **4a** and **4b** were prepared following a previously reported procedure shown in Scheme 1 [23]. As described before, 5 mL of an acetonitrile solution (MeCN, HPLC grade) containing 1 mmol of the appropriate *N*-propargylaniline (**1a**: R=CH_3, **1b**: R=Cl) and formaldehyde (**3**, 37% in methanol; 1.1 mmol) were added to a round bottom flask and stirred for 10 min. Then, 5 mL of a solution of $InCl_3$ (20 mol%) in MeCN was added. Stirring continued and, after 20 min, *N*-vinyl-2-pyrrolidinone (**2**, 1.1 mmol) was incorporated into the reaction mixture. The mixture was maintained under constant stirring at room temperature for 3–4 h, monitoring the reaction by TLC. When the reaction reached completion, it was diluted with water (30 mL) and extracted with ethyl acetate (3×25 mL). The organic layer was separated and dried with Na_2SO_4. The solvent was removed under vacuum and the

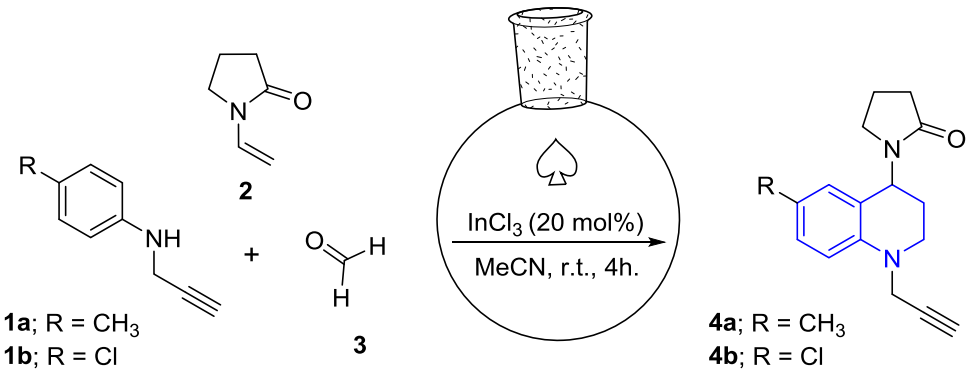

Scheme 1. Synthesis of *N*-propargyl-1,2,3,4-tetrahydroquinolines.

crude product obtained was purified by column chromatography and eluted with the appropriate mixture of petroleum ether and ethyl acetate. Translucent yellow plates of the pure tetrahydroquinolines **4a** and **4b**, of size and quality suitable for X ray diffraction studies, were obtained by slow evaporation of the petroleum ether:ethyl acetate solvent.

2.3. Characterization by spectroscopic techniques

2.3.1. N-*propargyl-6-methyl-4-(2′-oxopyrrolidin-1′-yl)-1,2,3,4-tetrahydroquinoline (4a)*

IR (ATR, cm^{-1}): 3212, 2951, 2890, 2097, 1667, 1500, 1332, 807, 707.

^{1}H-NMR (400 MHz, $CDCl_3$), δ: 1.92–2.04 (2H, m, 4'-H), 2.05-2.19 (2H, m, 3-H), 2.14 (1H, t, *J*=2.3 Hz, 13-H), 2.21 (3H, s, 6-CH3), 2.49 (2H, td, *J*= 8.1, 2.4 Hz, 3'-H), 3.07–3.29 (2H, m, 5'-H), 3.20–3.38 (2H, m, 2-H), 3.95 (1H, dd, *J*= 18, 2.4 Hz, 11-Ha), 4.04 (1H, dd, *J*= 18, 2.4 Hz, 11-Hb), 5.38 (1H, dd, *J*=8.7, 8.2 Hz, 4-H), 6.68 (1H, d, *J*= 8.3 Hz, 8-H), 6.72 (1H, s, 5-H), 6.98 (1H, ddd, *J*= 8.3, 1.5, 0.6 Hz, 7-H).

^{13}C-NMR (100 MHz, $CDCl_3$), δ: 18.42 (4'-C), 20.54 (6-CH3), 27.05 (3-C), 31.63 (3'-C), 41.12 (11-C), 43.9 (5'-C), 47.61 (2-C), 47.77 (4-C), 72.18 (13-C), 79.20 (12-C), 113.3 (8-C), 121.27 (4a-C), 127.66 (6-C), 128.7 (5-C), 129.21 (7-C), 143.21 (8a-C), 175.53 (2'-C).

MS (ESI-IT), *m/z* (%): 291.1 (56.19) $[M+Na]^+$, 531.1 (6.79) $[2M-CH_3+Na]^+$, 559.1 (100) $[2M+Na]^+$.

Anal. Calcd. for $C_{17}H_{20}N_2O$ (268.4 g/mol) C, 76.09; H, 7.51; N, 10.44 %. Found: C, 75.98; H, 7.41; N, 10.28 %.

2.3.2. N-*propargyl-6-chloro-4-(2′-oxopyrrolidin-1′-yl)-1,2,3,4-tetrahydroquinoline (4b)*

IR (ATR, cm^{-1}): 3209, 2954, 2932, 2887, 2845, 1670, 1488, 1422, 1164, 809.

^{1}H-NMR (400 MHz, $CDCl_3$), δ 1 1.97–2.06 (2H, m, 4'-H), 2.06–2.17 (2H, m,3-H), 2.16 (1H, t, *J*=2.4 Hz, 13-H), 2.48 (2H, m, 3'-H), 3.09-3.28 (2H, m, 5'-H), 3.24-3.43 (2H, m, 2-H), 3.92 (1H, dd, *J*= 18.3, 2.3 Hz, 11-Ha), 4.04 (1H, dd, *J*= 18.3, 2.3 Hz, 11-Hb), 5.36 (1H, dd, *J*= 9.2, 9.1 Hz, 4-H), 6.67 (1H, d, *J*= 8.9 Hz, 8-H), 6.85 (1H, dd, *J*=2.4, 0.7 Hz, 5-H), 7.10 (1H, dd, *J*=8.9, 2.6 Hz, 7-H).

^{13}C-NMR (100 MHz, $CDCl_3$), δ: 18.35 (4'-C), 26.52 (3-C), 31.4 (3'-C), 41.04 (11-C), 43.57 (5'-C), 47.59 (2-C), 47.61 (4-C), 72.46 (13-C), 78.62 (12-C), 114.34 (8-C), 122.94 (6-C), 123.11 (4a-C), 127.43 (5-C), 128.45 (7-C), 143.97 (8a-C), 175.60 (2'-C).

MS (ESI-IT), *m/z* (%): 291. 311.1 (100) $[M+Na]^+$, 599 (98.32) $[2M+Na]^+$, 886.2 (5.68) $[3M+Na]^+$.

Anal. Calcd. for $C_{16}H_{17}ClN_2O$ (288.7 g/mol) C, 66.55; H, 5.93; Cl, 12.28; N, 9.70%. Found: C, 66.48; H, 5.87; N, 12.08%.

2.4. Single crystal X ray diffraction study

Data collection: yellow-orange plates of compounds **4a** and **4b** with dimensions 0.66×0.61×0.34 and 0.43×0.41×0.37 mm^3, respectively, were selected under the microscope. They were mounted on MiTeGen Dual-Thickness 200 µm MicroLoops attached to a XYZ goniometer head. Intensity data from each crystal were collected in a Rigaku XtaLAB PRO diffractometer equipped with a Pilatus 200K detector and a SHINE (curved graphite monochromator) optics at 293 K. Mo*Kα* radiation (λ=0.71075 Å) from a sealed tube was used with the diffractometer operating at 50 kV and 40 mA. For compounds **4a** and **4b**, 1509 and 810 images, respectively, were collected in steps of 0.50° in ω with an exposure time per image of 30.00 s. The crystals did not experience decomposition upon exposure to X rays. Final unit cell parameters were determined from the positions of 17439 and 8499 reflections, respectively, in the approximate range $1.9° \leq \theta \leq 30°$ and were subsequently refined by least squares. Absorption, form, scale factor, among other corrections, were done by a multi-scan routine using a form function based on spherical harmonics. The CrystalClear-SM Expert [24] package was used for data collection and preliminary unit cell determination and CrysAlisPro [25] was used for final cell refinement, integration, and data reduction.

Structure determination and refinement: The structures were solved with SHELXT [26] and refined by full matrix least-squares with SHELXL [27], implemented within the OLEX2 software [28]. Positions and anisotropic displacement parameters were refined for all non-hydrogen atoms. Hydrogen atoms were identified in the difference Fourier map and refined using a riding model with their U_{iso} equal to $1.2U_{eq}$ of the carbon atom to which they are attached. The hydrogen atoms of the methyl groups were assigned $U_{iso}=1.5U_{eq}$ of the corresponding carbon atom. Graphic representations were produced with Diamond 3.0 [29] and Mercury [30], structure validation was accomplished with PLATON [31] and the program enCIFer [32] was used for CIF editing.

2.5. Hirshfeld surface analysis, energy frameworks and enrichment ratio

The calculated Hirshfeld surface mapped over the normalized contact distance d_{norm}, the associated two-dimensional fingerprint plots, and the energy frameworks were calculated using CrystalExplorer21 [33]. Hirshfeld surfaces mapped on d_{norm} use the function of normalized distances from a given point to the closest atom inside (d_i) and outside (d_e) the surface [34]. The blue, white, and red color conventions used for Hirshfeld surfaces show long, van der Waals, and short interatomic contacts, respectively.

The curvature surfaces (curvedness) and the shape index provide a greater chemical understanding of the packing of the structure [34]. A flat area on the surface is indicative of the possibility of $\pi\cdots\pi$ stacking in the crystal while a surface with a large curvature, highlighted as dark blue spots, is indicative of the absence of such stacking. The shape index is a qualitative interpretation of the shape of the surface. The shape index is differentiated by the blue color that indicates "bumps" associated with the donor of an intermolecular interaction and the red color that represents the "hollows" associated with the acceptors. The 2-D fingerprint plots provide a visual representation of the contribution of each combination of d_e and d_i on the surface.

The calculation of energy frameworks of the interactions includes the sum of four energy components comprising electrostatics (E_{ele}), polarization (E_{pol}), dispersion (E_{dis}) and exchange repulsion (E_{rep}) [33–34]. The energy was calculated using the molecular wavefunction at the B3LYP/6–31G(d,p) level within a radius of 3.8 Å. Neighboring molecules within this shell are generated by symmetry operations. The graphical representation of the individual energy components of the interactions consists of cylinders joining the centroids of interacting molecular pairs; the radius of the cylinders is proportional to the magnitude of the interaction energy.

The enrichment ratio (E_{XY}) of a pair of elements (X, Y) is defined as the ratio between the ratio of actual contacts in the crystal and the theoretical ratio of random contacts [35]. For pairs of elements that have a high propensity to form contacts in the crystal $E_{XY} > 1$ while an E_{XY} value < 1 indicates those that tend to avoid contacts. The enrichment ratios were determined using the MoProViewer program [36].

2.6. Molecular Dynamics Simulations (MDs)

MDs were performed to study the interactions of both **4a** and **4b** (*R* and *S* isomers) with MAO-B. First, the crystal structure of MAO-B in a complex with the rasagiline covalent inhibitor drug (PDB code: 1S2Q) [23] was used as reference, and the *N*-propargyl

adducts (4a-(*S*)-FAD, 4a-(*R*)-FAD, 4b-(*S*)-FAD, and 4b-(*R*)-FAD) were manually assembled following the proposed mechanism of the MAO-B irreversible inhibition of rasagiline and seleginine [17]. Second, the five MAO-B complexes (rasagiline-FAD, 4a-(*S*)-FAD, 4a-(*R*)-FAD, 4b-(*S*)-FAD, and 4b-(*R*)-FAD) were prepared using the Protein preparation wizard from the Maestro Suite [37]. Then, the complexes were optimized and subjected to a conjugate gradient energy minimization and 270 ns MDs in Desmond using the OPLS3 force field [38–39].

To build each system, the complexes were solvated with a pre-equilibrated SPC water model (~15500 water molecules). The systems were neutralized by adding Na^+ counter ions to balance the net charge of the systems and NaCl at a concentration of 0.15 M was added to simulate physiological conditions. Each system was subjected to the default Desmond relaxation protocol, and then equilibrated with a spring constant force of 5.0 kcal × mol^{-1} × $Å^{-2}$ applied to the MAO-B secondary structure, and 5.0 kcal × mol^{-1} × $Å^{-2}$ applied to the FAD co-factor, for 20 ns at constant pressure (1 atm) and temperature (300 K). The isothermal-isobaric ensemble and the Nosé–Hoover method were used with a relaxation time of 1 ps applying the MTK algorithm [40], with a timestep of 2 fs. Then, the last frame was taken, and a second MDs was performed for 250 ns with a spring constant force of 1.0 kcal × mol^{-1} × $Å^{-2}$ applied to the MAO-B secondary structure, and 0.5 kcal × mol^{-1} × $Å^{-2}$ applied to the FAD co-factor. The last 250ns-MDs were used for further analyses here. The restrictions applied here were used to keep the binding site of the *N*-propargyl as close as possible to that described in the MAO-B crystal (PDB code: 1S2Q) in complex with rasagiline (covalently bound to FAD). No restrictions were applied to the MAO-B backbone and side chains of the residues to allow the binding pockets to fit each ligand.

3. Results and discussion

3.1. Crystal structure *of* N-*propargyl-6-methyl-4-(2′-oxopyrrolidin-1′-yl)-1,2,3,4-tetrahydroquinoline (4a) and* N-*propargyl-6-chloro-4-(2′-oxopyrrolidin-1′-yl)-1,2,3,4-tetrahydroquinoline (4b)*

Crystal data, experimental details and refinement results are summarized in Table 1. Bond lengths and bond angles are presented in the Supplementary Material, Table S1, and torsion angles are given in Table S2.

3.1.1. Molecular structure

The asymmetric units of **4a** and **4b** consist of one molecule of the compound. Fig. 2a and 2b show the molecules with their atom and ring labeling scheme. Rings B (C1-C4/C9/N1) and C (C4-C9) are almost coplanar in both compounds. The angle B/C in **4a** is 6.48(6)° and 5.44(10)° in **4b**. The five-member ring (Ring A: N2/C13-C16) is almost perpendicular to rings B and C. In **4a** the A/B and A/C angles are 78.09(7)° and 84.56(7)°, respectively, while in **4b** they are 76.88(11)° and 82.21(10)°, respectively.

The torsion angle N2-C3-C4-C5 is similar in both compounds, -24.24(15)° and -24.6(2)° for **4a** and **4b**, respectively. However, the C16-N2-C3-C4 torsions differ by almost 3° (-74.39(14)° and -77.00(18)°, respectively). The ring puckering analysis carried out with PLATON [31] indicates Ring A is twisted on C15-C16 in both compounds. The analysis of Ring B is not conclusive but, based on the values of θ and ϕ [**4a**: 46.17(15)° and 115.4(2); **4b**: 47.5(2)° and 116.3(3)°)], the rings have conformations between half-chair and envelope. In **4a**, the angle N1-C10-C11 is 113.55(12)° and the propargyl group makes an angle of 85.47(10)° with the best plane trough Rings B/C. The corresponding values in **4b** are 113.14(16)° and 87.21(15)°.

In spite of the differences, the molecules are almost exactly superimposable. The RMDS values, calculated with Mercury [30], for the superposition are 0.0620 without allowing flexibility and 0.0578 allowing flexibility. The superposition is shown in Fig. 2c.

A search of the Cambridge Structural Database (CSD), version 2021.2 [41] for *N*-propargyl-hydroquinolines resulted in thirteen hits of which nine are the most closely related compounds (Table S3). The analysis of the geometry of the *N*-propargyl group (N1-C10-C11≡C12) in thirty *N*-propargyl substituted six-member rings indicates that the mean N1-C10, C10-C11, and C11≡C12 bonds distances are 1.475, 1.467, and 1.175 Å and the mean values for the N1-C10-C11 and C10-C11≡C12 angles are 112.49° and 177.43°. Therefore, the values observed in **4a** [1.4548(16) Å / 1.477(2) Å / 1.174(2) Å and 113.55(12)° / 177.68(15)°] and in **4b** [1.455(2) Å / 1.475(3) Å / 1.173(3) Å and 113.14(16)° / 177.42(19)°] are within the values expected for this group.

3.1.2. Intramolecular hydrogen bonds

Table 2 summarizes the hydrogen bonds observed in **4a** and **4b**. In both compounds, there are two intramolecular hydrogen bonds involving the O and N of the oxopyrrolidinyl ring. As depicted in Fig. 3, both types of intramolecular hydrogen bonds are represented by the graph set symbol S(5) [42–43].

These intramolecular hydrogen bonds are considered weak based on their distances and angles. Gilli and Gilli [44] and Desiraju and Steiner [45] point out that H···A (A = Acceptor) distances in H···O and H···N hydrogen bonds in the range of 2.0 to 3.0 Å and C—H···A angles of 90 to 180° are considered weak contacts with bond energies usually around 4 Kcal mol^{-1}. On the other hand, molecular dynamics simulations carried out on a similar hydrogen bond motif present in a methylimidazolium-methylsulfate ionic liquid indicate that the enthalpy of formation of these hydrogen bonds is -5 kJ mol^{-1} [46].

A search of the CSD [41] and a statistical analysis with Mercury [30] of compounds containing an oxopyrrolidinyl ring bonded to a tetrahydroquinoline indicate that the intramolecular C—H···O and C—H···N hydrogen bonds observed in **4a** and **4b** are in the range of distances and angles of the compounds reported in the database (see Table S4 of the Supplementary Material). The C—H···O contacts in **4a** and **4b** are 2.45 and 2.44 Å and have angles of 103 and 102°, respectively. For the C—H···N the corresponding values are 2.54 and 2.55 Å and 103 and 101°. The mean values for the compounds in the database, as can be seen in Table S4, are 2.42 Å, 2.58 Å, 105°, and 99.5°, respectively. Although weak, these contacts play an important role in stabilizing the molecular conformation and the crystal packing of both compounds.

3.1.3. Intermolecular hydrogen bonds

Fig. 4 shows the sequence of intermolecular hydrogen bonds in **4a** and **4b**, respectively. Both compounds display a helical arrangement of medium strength hydrogen bonds between the O atom of the oxopyrrolidinyl ring (O1) and the propargyl hydrogen (H12) involving molecules related by the 2_1-screw along the *b*-axis (Table 2). In addition, molecules related by translation along the *b*-axis are connected by weak interactions between C10—H10A and C17 of the methyl group on ring C of compound **4a** (Fig. 4a). This interaction is replaced by a stronger C10—H10A···Cl1 hydrogen bond in compound **4b** (Fig. 4b). The hydrogen bonding scheme can be described as a sequence of alternating motifs represented by a fourth-order graph set with symbol $R_5^4(22)$ [42–43].

3.1.4. C–H···π Interactions

Two types of C–H···π interactions are observed in compounds **4a** and **4b**: one involves the aromatic ring (ring C) and one in-

Table 1
Crystal data and details of the structure determination of compounds **4a** and **4b**.

Crystal data		
	Compound 4a	Compound 4b
CCDC Deposition Number	2082183	2082184
Formula	$C_{17}H_{20}N_2O$	$C_{16}H_{17}ClN_2O$
Formula Weight, M_r	268.35	288.76
Crystal System	Monoclinic	Monoclinic
Space group	$P2_1/c$ (No. 14)	$P2_1/c$ (No. 14)
a [Å]	12.2048(4)	12.1080(6)
b [Å]	10.2934(3)	10.3426(3)
c [Å]	12.9760(5)	12.9506(7)
β [°]	116.827(5)	116.548(7)
V [Å^3]	1454.71(11)	1450.78(14)
Z	4	4
D_c [g cm^{-3}]	1.225	1.322
μ(Mo Kα) [mm^{-1}]	0.077	0.260
Crystal shape, color	Plates, yellow	Plates, yellow
Crystal Size [mm^3]	0.34×0.61×0.66	0.37×0.41×0.43
Data Collection		
Temperature [K]	293	293
Radiation [Å]	Mo$K\alpha$ 0.71075	Mo$K\alpha$ 0.71075
θ range [°]	$1.9 \leq \theta \leq 30.2$	$1.9 \leq \theta \leq 29.4$
Dataset	-15:16; -14:14; -17:17	-16:13; -14:13; -16:17
Tot. data, Uniq. data, R_{int}	25791, 3947, 0.044	13774, 3466, 0.024
Observed data [$I > 2\sigma(I)$]	3335	2721
Refinement		
Nref, Npar	3947, 182	3466, 181
$R[F^2 > 2\sigma(F^2)]$, $wR(F^2)$, S	0.0453, 0.1388, 1.05	0.0400, 0.1158, 1.13
$\Delta\rho_{min}$ / $\Delta\rho_{max}$ [e Å^{-3}]	-0.19, 0.21	-0.44, 0.34

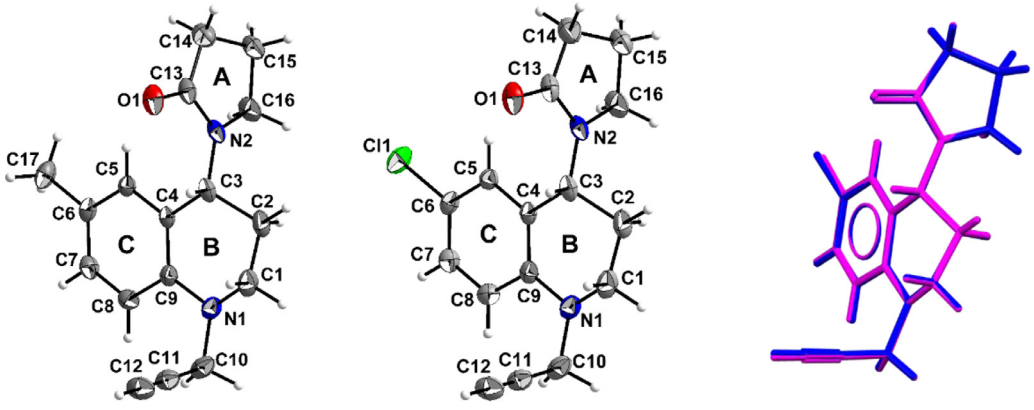

Fig. 2. (a) Molecular structure of compound **4a** and (b) of compound **4b**, showing the atom and ring labeling scheme. Ellipsoids are drawn at the 30% level of probability. (c) Superposition of the molecules of **4a** (magenta) and **4b** (blue). The hydrogen atoms of the methyl group of **4a** are omitted.

volves the triple bond of the propargyl moiety (Fig. 5). The geometries of these interactions are summarized in Table 3. Fig. 5a and 5b show the sequence of C-H···π(Cg3) (dark-red) interactions between molecules related by the *c*-glide plane. Fig. 5c and 5d depict the geometry of C–H···π(C≡C) contacts showing that the interactions in **4b** are shorter than in **4a**. In addition, molecules related by translation are connected through C–H···CH_3 (**4a**) or C–H···Cl (**4b**) hydrogen bonds along the ***b***-axis and by C–H···π(C≡C) interactions with inversion related molecules to form tapes in the *bc* plane as represented in Fig. 5e and 5f.

3.1.5. Packing arrangement

The structures may be viewed as a stacking of columns formed by inversion-related helices. Each helix is formed by molecules related by the 2_1-screw axis along *b* and the connectivity within the helix is due to hydrogen bonds between the propargyl moiety and the oxygen atom of the oxopyrrolidinyl ring (C12—H12···O1), the C10—H10A···C17 for **4a** and C10—H10A···Cl1 for **4b** interactions, and the C—H···π(Cg3) interactions. The inversion-related helices are interpenetrated and form columns that run along *c*, connected by the C—H···π(C≡C) contacts which occur approximately along the [101] direction. Fig. 6a and 6b present views of the structures along the *b*- and *c*-axes (depicted only for **4b**). In Fig. 6c and 6d, the molecules are colored based on the symmetry operation.

3.2. Hirshfeld surface analysis, energy frameworks, and enrichment ratio

The Hirshfeld surfaces [34] of both compounds are similar (Fig. 7a and 7d). The surfaces of the structures reveal two intense red spots corresponding to the hydrogen bonding interaction C—H···O between the propargyl group and the oxygen of the oxopyrrolidinyl fragment. Additionally, two small red spots are observed

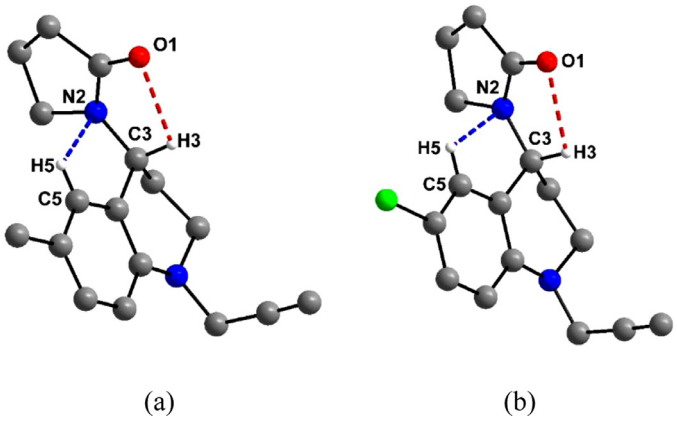

Fig. 3. Intramolecular hydrogen bonds in (a) compound **4a** and (b) compound **4b**. All intramolecular hydrogen bonds are represented by the graph set symbol S(5). Hydrogen atoms not involved in hydrogen bonding have been omitted for clarity.

Table 2
Hydrogen bond lengths (Å) and bond angles (°).

D-H···A	D-H(Å)	H··A(Å)	D-A(Å)	D-H··A(º)
Compound 4a				
C3-H3···O1	0.9800	2.4500	2.8389(16)	103.00
C5-H5···N2	0.9300	2.5400	2.8772(13)	102.00
C10-H10A···C17^{i}	0.9700	2.9000	3.7034(1)	166.00
C12-H12···O1^{ii}	0.9300	2.3000	3.221(2)	173.00
Compound 4b				
C3-H3···O1	0.9800	2.4400	2.829(2)	103.00
C5-H5···N2	0.9300	2.5500	2.8783(17)	101.00
C10-H10A···Cl1^{iii}	0.9700	2.8200	3.5931(16)	137.00
C12-H12···O1^{iv}	0.9300	2.2900	3.2080(3)	170.00

Symmetry Codes: i) x, -1+y, z; ii) 1-x, 1/2+y, 1/2-z; iii) x, 1+y, z; iv) 1-x, 1/2+y, 3/2-z.

(yellow circles) that show the participation of the triple bond of the propargyl as an acceptor in an H···π interaction with a hydro-

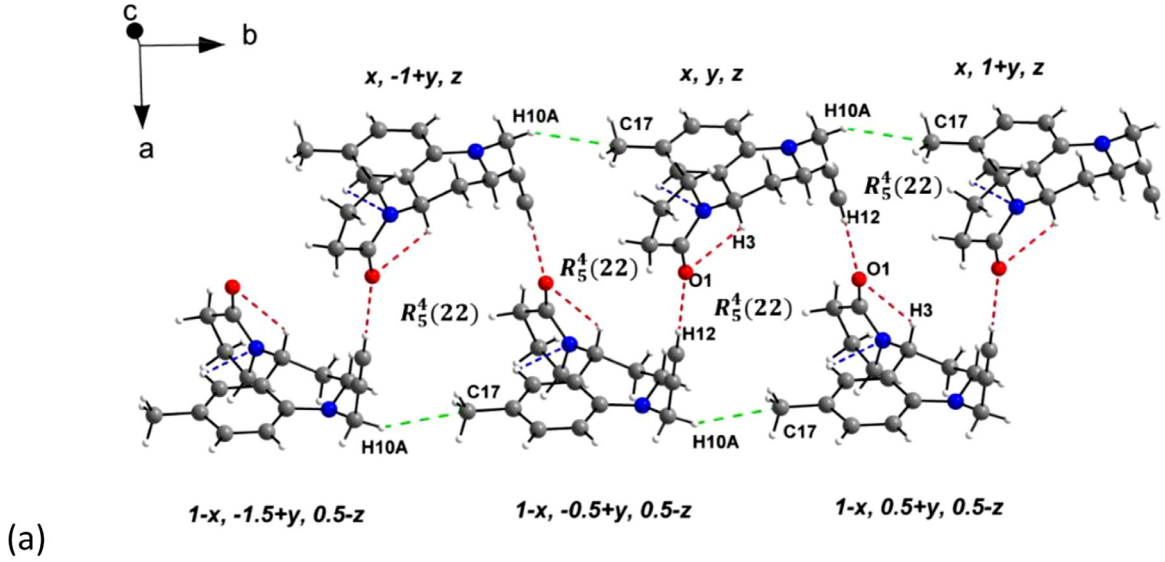

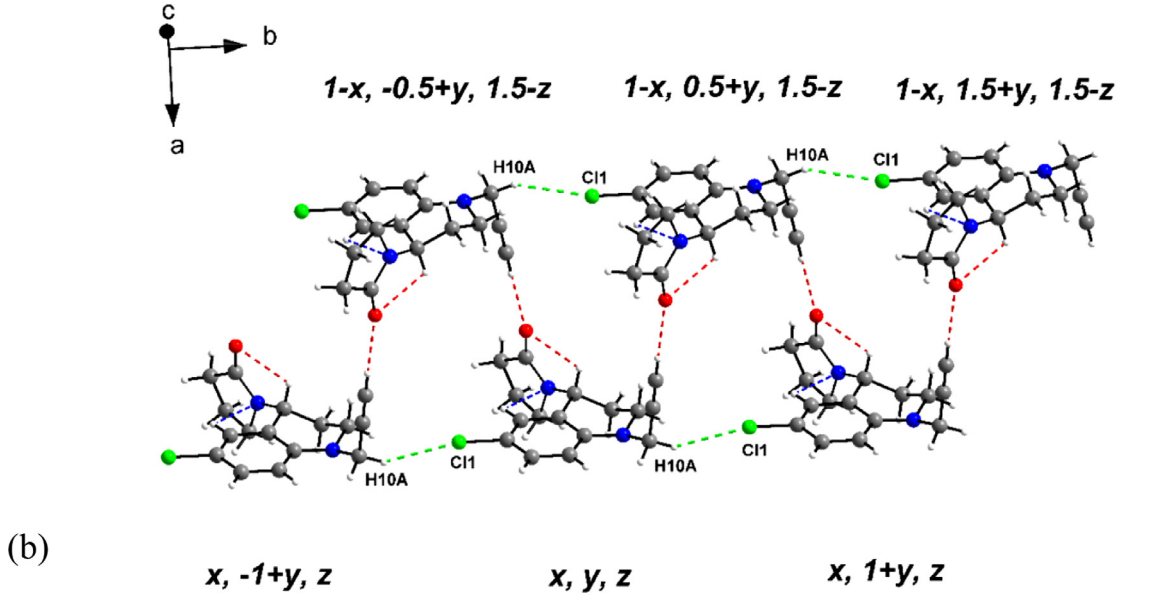

Fig. 4. View of the hydrogen bonding scheme for (a) compound **4a** and (b) **4b.**

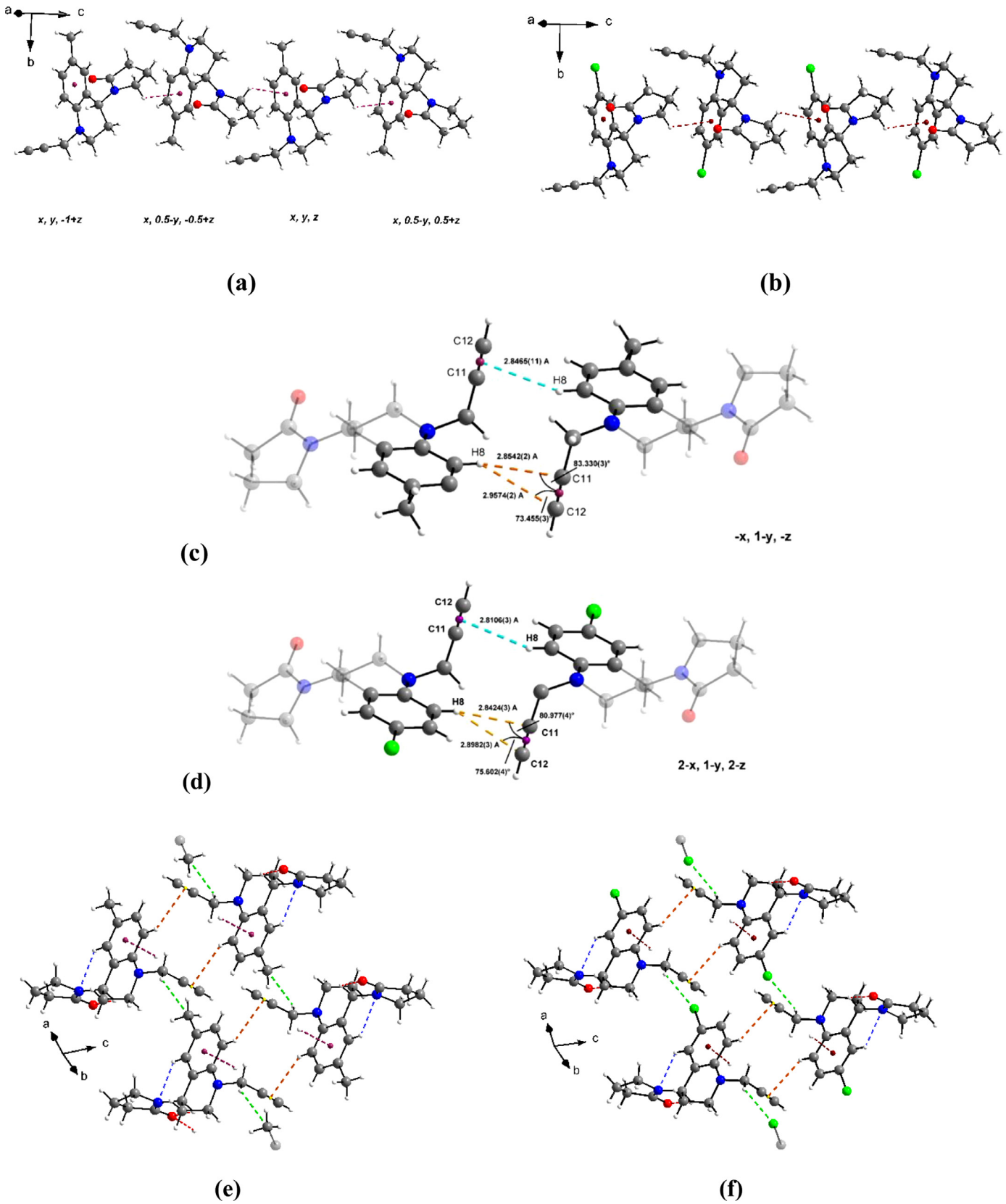

Fig. 5. Views of C-H···C, C-H···Cl, and C-H···π interactions present in compounds **4a** and **4b**. C-H···π(Cg3) interactions in (a) compound **4a** and (b) compound **4b**. (c) and (d) Geometry of the C-H···π(C≡C) interactions in **4a** and **4b**. (e) C-H···π(Cg3) (dark red), C-H···π(C≡C) (orange), and C-H···C (green) interactions in **4a**. (f) C-H···π(Cg3), C-H···π(C≡C) and C-H···Cl (green) interactions in the structure of **4b**.

Table 3
Geometry of C–H···π(ring) and C–H···π(C≡C) interactions in **4a** and **4b** calculated with PLATON [31].

X–H···π	Geometry parameters[a]			Symmetry Code
Compound 4a				
C16–H16B···Cg3	***d***	***γ***	**H-Perp**	x,1/2-y,1/2+z
	2.86 Å	10.60°	2.81 Å	
	X-H···Cg	**X···Cg**	**X-H, π**	
	118°	3.429(2) Å	39°	
C18—H18···π(C≡C)	**H8···π**	**H8···C11**	**H8···C12**	-x, 1-y, -z
	2.847(1) Å	2.8542(2) Å	2.9574(2) Å	
	H···C11-π		**H···C12-π**	
	83.330(3)°		73.455(3)°	
Compound 4b				
C16–H16B···Cg3	***d***	***γ***	**H-Perp**	x,1/2-y,1/2+z
	2.86 Å	14.57°	-2.77 Å	
	X-H···Cg	**X···Cg**	**X-H, π**	
	116°	3.395(3) Å	40°	
C18—H18···π(C≡C)	**H8···π**	**H8···C11**	**H8···C12**	2-x, 1-y, 2-z
	2.8106(3) Å	2.8424(3) Å	2.8982(3) Å	
	H···C11-π		**H···C12-π**	
	80.977(4)°		75.602(4)°	

[a] Cg3 is the centroid of ring C, defined by atoms C4/C5/C6/C7/C8/C9 and π(C≡C) is the midpoint of the C11≡C12 bond. The geometry of the contacts is defined by the following parameters: ***d*** = H···Cg distance; ***γ*** = angle between Cg-H vector and ring C normal; **H-Perp** = perpendicular distance of H to ring plane C; **X-H···Cg** = X-H-Cg angle (°); **X···Cg** = distance of X to Cg; **X-H, π** = angle of the X-H bond with the π-plane.

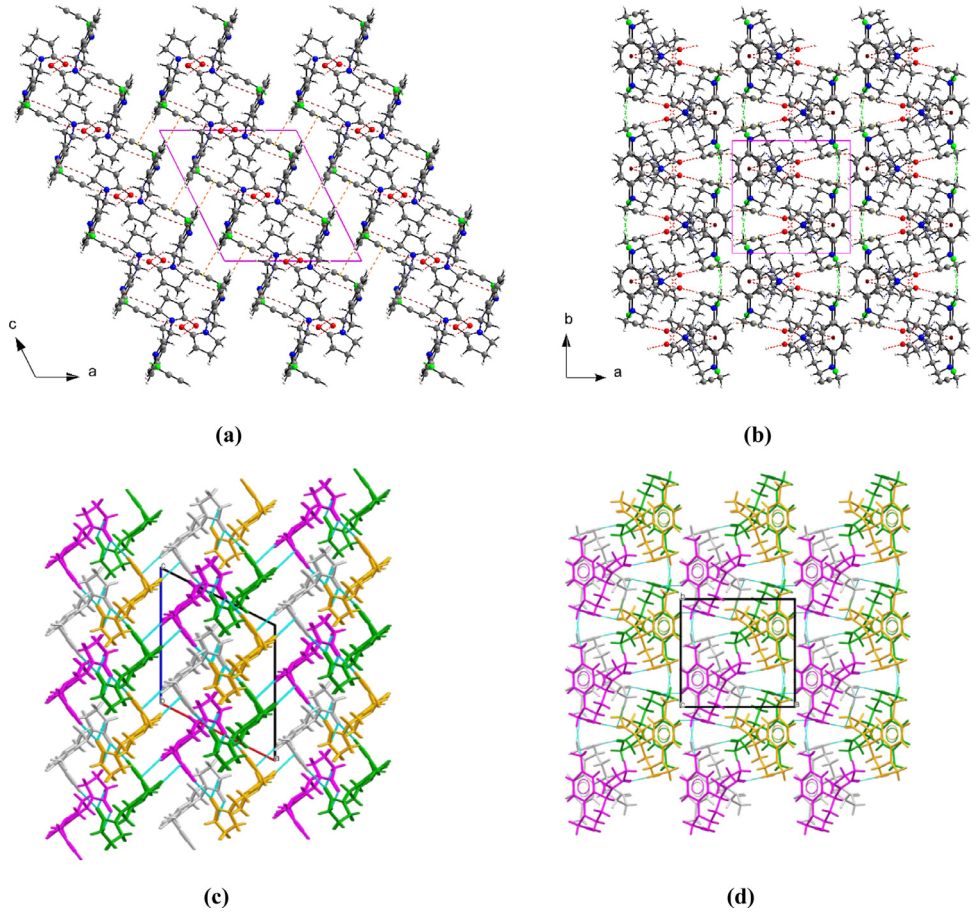

Fig. 6. (a) View down the *b*-axis and (b) down the *c*-axis of the packing arrangement of **4a** and **4b** (depicted only for **4b**). (c) and (d) show the same packing diagrams colored according to symmetry operators. Light grey: *x, y, z*; green: *-x, 1/2+y, 1/2-z* (2_1 screw axis); gold: *-x, -y, -z* (Inversion); magenta: *x, 1/2-y, 1/2+z* (*c*-glide plane).

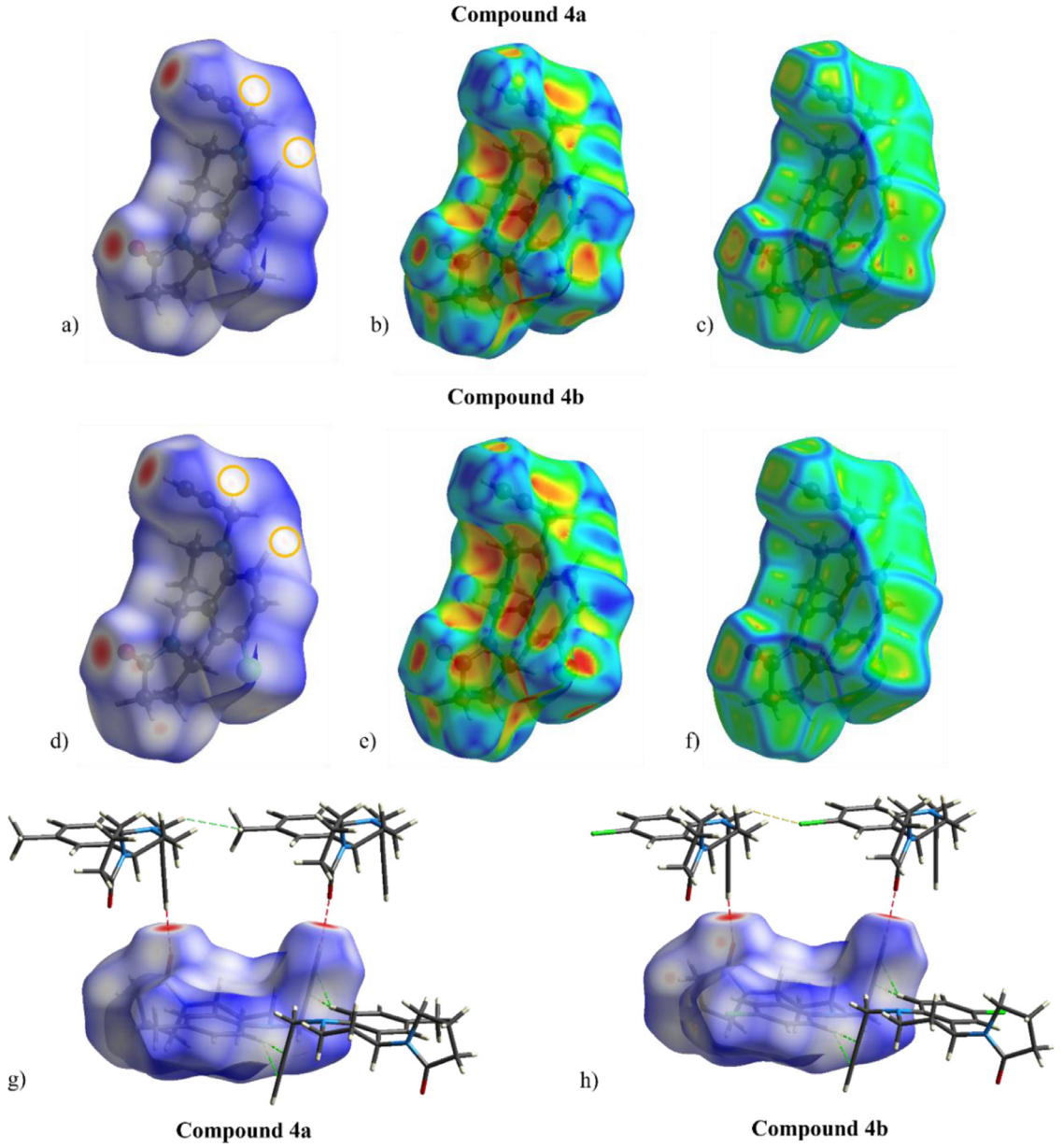

Fig. 7. Hirshfeld surface for compounds **4a** and **4b** mapped with d_{norm} (a and d), shape index (b and d), and curvedness (c and f). The red spots in a) and d) indicate the shortest interactions; g) and h) show neighboring molecules connected by C—H(propargyl)···O and C—H···π(propargyl) interactions in both compounds.

gen of the benzene ring as shown in Fig. 7g and 7h. The surface of compound **4b** shows a light spot on the chlorine atom indicating that it participates in an intermolecular interaction. The shape index representations (Fig. 7b and 7e) show red areas for the H···π interactions between the benzene rings and the propargyls present in both structures. The curvedness plots do not show flat areas where the aromatic rings are located (Fig. 7c and 7f), which indicates that the presence of π···π interactions in the packing can be discarded. On the other hand, planarity is observed on the surface where the propargyl and the carbonyl of the oxopyrrolidinyl are located, indicating a slight stacking in these groups due to the C—H···O hydrogen bond where they participate.

Fig. 8 shows the fingerprint plots [34] calculated with CrystalExplorer21 [33] for compounds **4a** and **4b** as explained in Section 2.5. Fig. 8a and 8f represent the overall plots and the interactions between pairs of atom types are shown in Fig. 8b-e and 8g-m for **4a** and **4b**, respectively. In the structures of **4a** and **4b** the greatest contributions on the surfaces correspond to the H···H contacts (63.4% and 46.3%), indicating the existence of short interactions, that may be repulsive or attractive. The H···π interactions (contributing 24.8% and 25.4% for **4a** and **4b**, respectively) and O···H hydrogen bonds (9.9% and 10.0%) follow in importance. In compound **4b** the contribution of the Cl···H bond is evident with a value of 14.9%.

The interaction energies between the central molecule and neighboring molecules in the 3.8 Å radius are shown in Table S5 and the graphical representation is shown in Fig. S1 of the Supplementary Material. In the two structures the most important stabilization energies are observed in molecules that are located at approximately 6-8 Å from the central molecule with symmetry operations -x, -y, -z and x, -y+1/2, z+1/2. They are followed by the interactions of neighboring molecules with operations -x, y+1/2, -z+1/2. The other energies with a significant contribution to the stabilization of the structure are present in neighboring molecules at a distance between 9-10 Å. Table S5 shows that the dispersive energy dominates over the electrostatic energy.

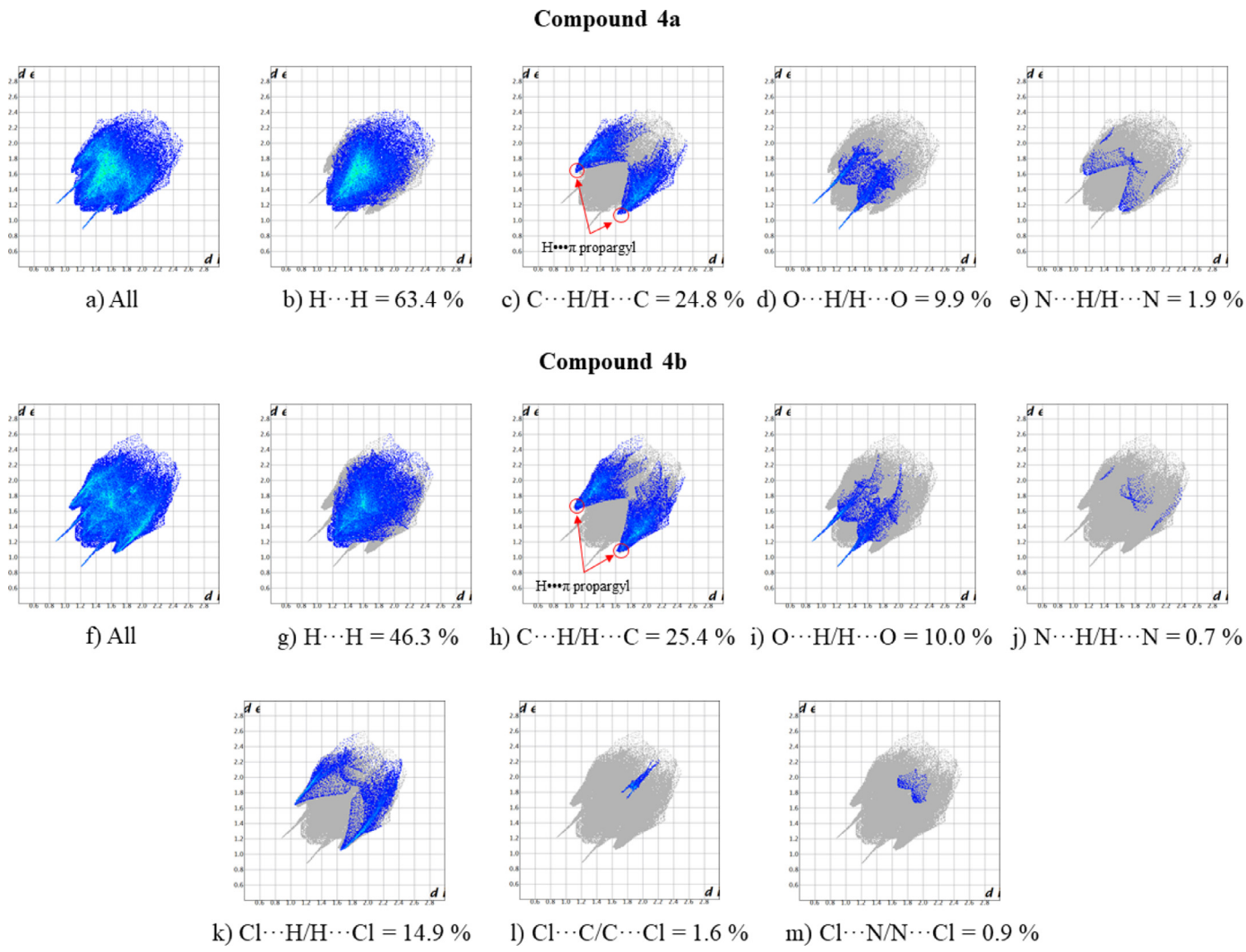

Fig. 8. Fingerprint plots for compounds **4a** and **4b** showing all contacts (a and f) and those for specific contacts (b–e and g–m). The percentage of surface area included is shown for each plot.

In compounds **4a** and **4b** the H···O bond contributes to stabilization with energies of -16.6 kJ/mol and -15.5 kJ/mol respectively, represented as diagonal cylinders in the dimer chain of molecules seen along the **b**-axis (Fig. 9a, 9b, and 9c). The dimer chains are connected by the short H···π interactions that involve the propargyls and have significant energy values of -19.5 kJ/mol in compound **4a** and -22.3 kJ/mol in **4b** (see Table S5). As shown by the topology of the energy frameworks, this interaction is observed in the diagonal between the chains when projected onto the **ac** plane. The view down the c-axis (Fig. 9d, 9e, and 9f) shows that the strongest interactions occur in a zig-zag fashion along the b-axis.

The different interactions were also evaluated using the E_{XY} enrichment ratio, calculated with the program MoPro [35–36]. The highest contributions of the Hirshfeld surface correspond to the H···H interactions. However, the E_{HH} values (Table 4) indicate that dispersive forces are not very favored in the packing. In the structure of compound **4a**, the E_{XY} values of the O···H contacts (E_{OH} = 1.42), C···H (E_{CH} = 1.28) and N···H (E_{NH} = 1.18) indicate they are the most enriched, showing the propensity to form these interactions. The contribution of N···C interactions is small while C···C and O···C are not very favored; on the other hand, in compound **4b**, the most enriched contacts are Cl···N (E_{ClN} = 5.13), O···H (E_{OH} = 1.65), C···H (E_{CH} = 1.36) and Cl···H (E_{NH} = 1.28). In this case the N···C (E_{NC} = 1.08) contact is slightly favored while the least favored are those with $E_{XY} < 1$. In both structures the N···N, N···O, and O···O contacts are completely avoided with E_{XY} = 0.0.

3.3. Characterization of the N-propargyl binding mode in MAO-B through MDs

To study the interactions of both **4a** and **4b** with MAO-B, we manually assembled the adducts 4a-(*S*)-FAD, 4a-(*R*)-FAD, 4b-(*S*)-FAD, and 4b-(*R*)-FAD using as reference the structure of MAO-B in complex with the rasagiline covalent inhibitor drug, as well as the reported mechanism of the MAO-B irreversible inhibition of rasagiline and seleginine [17]. In Fig. 10 the 2D-structures of the proposed adducts used in this work are shown.

The five complexes were subjected to MDs to study how different *N*-propargyl derivatives interact with MAO-B when they are covalently bound to the FAD. Fig. 11a shows how the Root-mean-square deviations (RMSDs) of the position for all backbone atoms of the MAO-B do not change more than 0.5 Å along the 250ns-MDs. This is mainly due to the restriction applied to the atoms of the secondary structure, and also to the stability of the crystal during the simulation. The results allow us to be sure that the binding site of rasagiline coming from the crystallographic 3D-structure did not suffer major conformational changes, thus allowing us to study

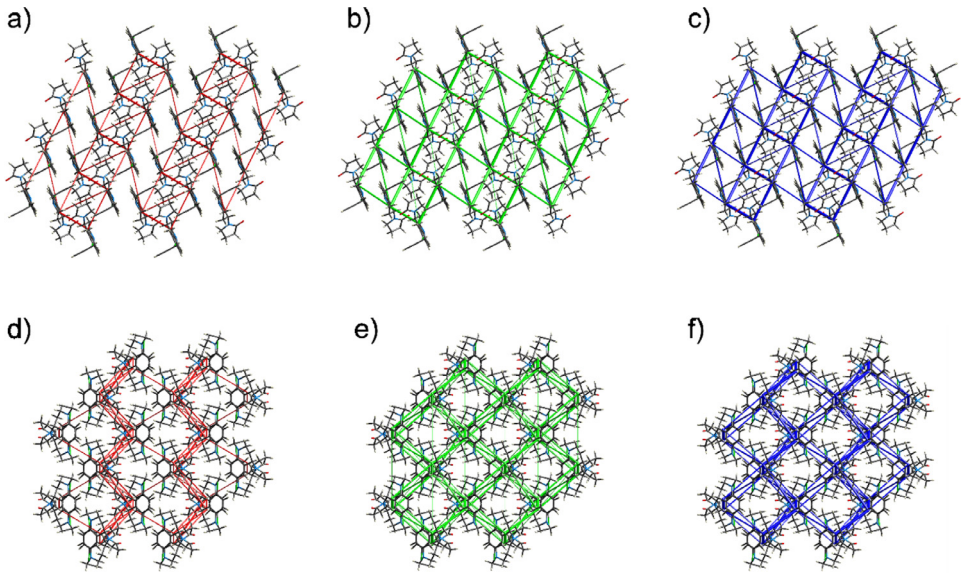

Fig. 9. Energy frameworks calculated for compound **4b** viewed down the *b*-axis (a-c) and down the *c*-axis (d-f). The energy frameworks are represented within 2×2×2 unit cells. The radii of the cylinders were scaled to 70 arbitrary units with a cut-off value of 10 kJ mol^{-1}. E_{ele}, E_{dis}, and E_{tot} are represented (left to right) in red, green, and blue, respectively.

Table 4
Hirshfeld contact surfaces, derived random contacts and enrichment ratios for **4a** and **4b**. The data values obtained from *CrystalExplorer* are written in italics in the table. The enrichment ratios were not computed when the 'random contacts' were lower than 0.9%, as they are not meaningful.

	Compound 4a				Compound 4b				
Atoms	H	C	N	O	H	C	N	O	Cl
H	*66.4*	Contacts		*%*	*46.3*	Contacts			*%*
C	*24.8*	*0.0*	-	-	*24.4*	*0.0*	-	-	-
N	*1.9*	*0.0*	*0.0*	-	*0.7*	*0.3*	*0.0*	-	-
O	*9.9*	*0.0*	*0.0*	*0.0*	*10.0*	*0.0*	*0.0*	*0.0*	
Cl	/	/	/	/	*14.9*	*1.6*	*0.9*	*0.0*	*0.0*
Surface %	66.77	27.27	1.08	4.88	56.78	26.05	0.96	5.00	11.21
H	45.38	Random Contacts %			32.37	Random Contacts %			
C	35.96	7.12	-	-	29.05	6.51	-	-	-
N	1.39	0.55	0.01	-	1.06	0.47	0.01	-	-
O	6.63	2.63	0.10	0.24	5.78	2.60	0.09	0.26	-
Cl	/	/	/	/	13.16	5.91	0.22	1.18	1.34
H	0.86	-	Enrichment		0.74	-	-	Enrichment	
C	1.28	0.45	-	-	1.36	0.44	-	-	-
N	1.18	0.76	0.0	-	0.23	1.08	0.00	-	-
O	1.42	0.17	0.0	0.0	1.65	0.20	0.00	0.00	-
Cl	/	/	/	/	1.28	0.83	5.13	0.11	0.06

alterations at the level of the side chains of the residues that interact directly with the ligands. The changes of the RMSDs for each ligand (Fig. 11) show that rasagiline remains very stable during the entire simulation. Nevertheless, the other ligands show minor conformational changes, in order to quickly stabilize and properly fit into the binding site. It is worth mentioning that during the simulation the part of the adduct that is "re-adjusted" is only the ligand portion, and that the FAD remains quite stable throughout the simulation (Fig. 11b).

We also analyzed the chemical nature of the drug interaction with MAO-B over the time of the simulations. The data were categorized and summarized in two types: Contact interaction frequencies at 4 Å for each ligand (Fig. 12a), and also as interaction fractions mainly distributed as hydrophobic, water bridges and hydrogen bonds (Fig. 12b). The heat-map allows to identify that residues G58, Y60, F168, L171, C172, I198, I199, Q206, Y326, F434, Y398, and Y435 are forming the binding site of all the *N*-propargyl compounds, a binding that is governed mainly by hydrophobic contacts (Fig. 12 and Fig. 13) such as the C-H···π interactions which occur in **4a** and **4b**. This indicates that although ligands **4a** and **4b** are more voluminous than rasagiline, they interact in a similar way with MAO-B once they are covalently bound to the FAD. There are also certain interactions mediated by hydrogen bonds and water bridges, mainly with the Q206 and Y326 residues (Figs. 12b and 13).

3.4. Chemical synthesis and spectroscopic analysis

The synthesis of compounds was carried out through the cationic version of the Povarov reaction described earlier [23]. The desired compounds were obtained in high yields (95% for **4a** and 91% for **4b**). The compounds (obtained as a racemic mixture) were

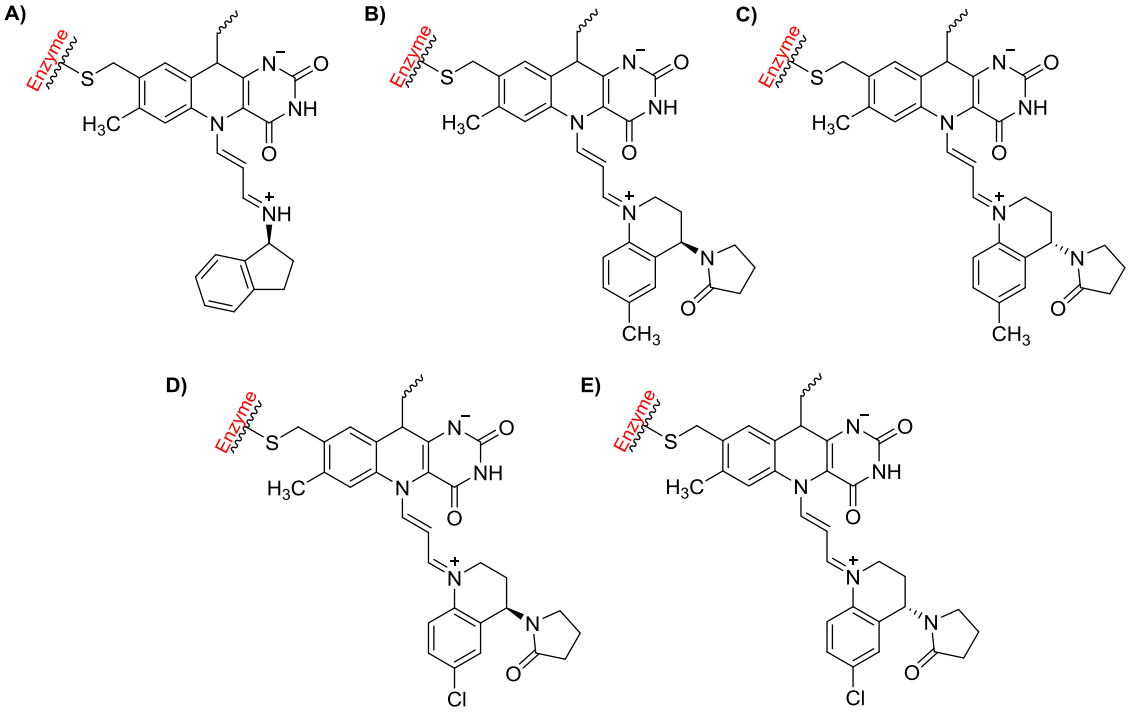

Fig. 10. 2D-structures of the proposed adducts. A) Rasagiline-FAD. B) 4a-(*S*)-FAD. C) 4a-(*R*)-FAD. D) 4b-(*S*)-FAD. E) 4b-(*R*)-FAD.

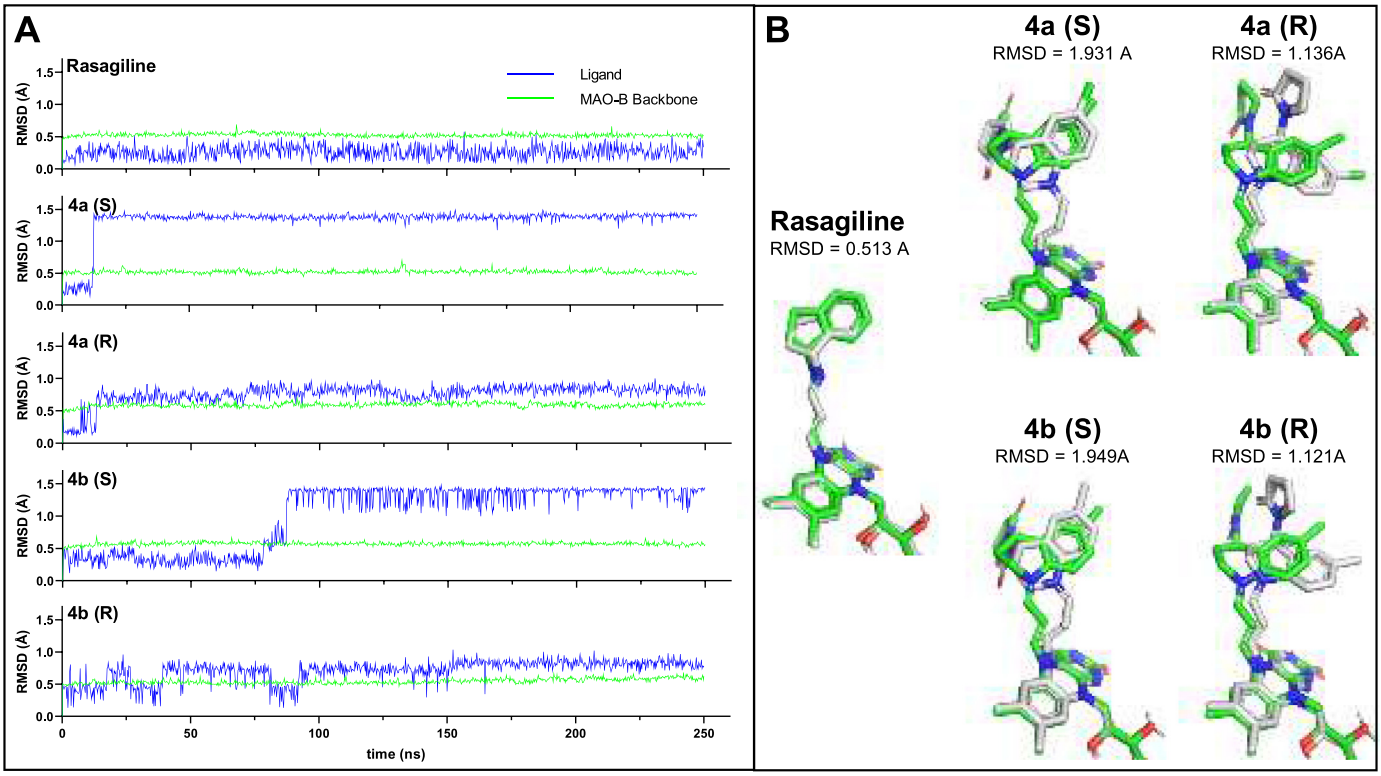

Fig. 11. a) Time dependence of the RMSD for Ligand atoms (blue) and MAO-B backbone atoms (green) during the 250 ns unrestrained MDs for Rasagiline, 4a-(*S*), 4a-(*R*), 4b-(*S*) and 4b-(*R*). b) Comparison between the starting conformations (green) and the final conformations (gray) of Rasagiline, 4a-(*S*), 4a-(*R*), 4b-(*S*) and 4b-(*R*) in the 250 ns unrestrained MDs.

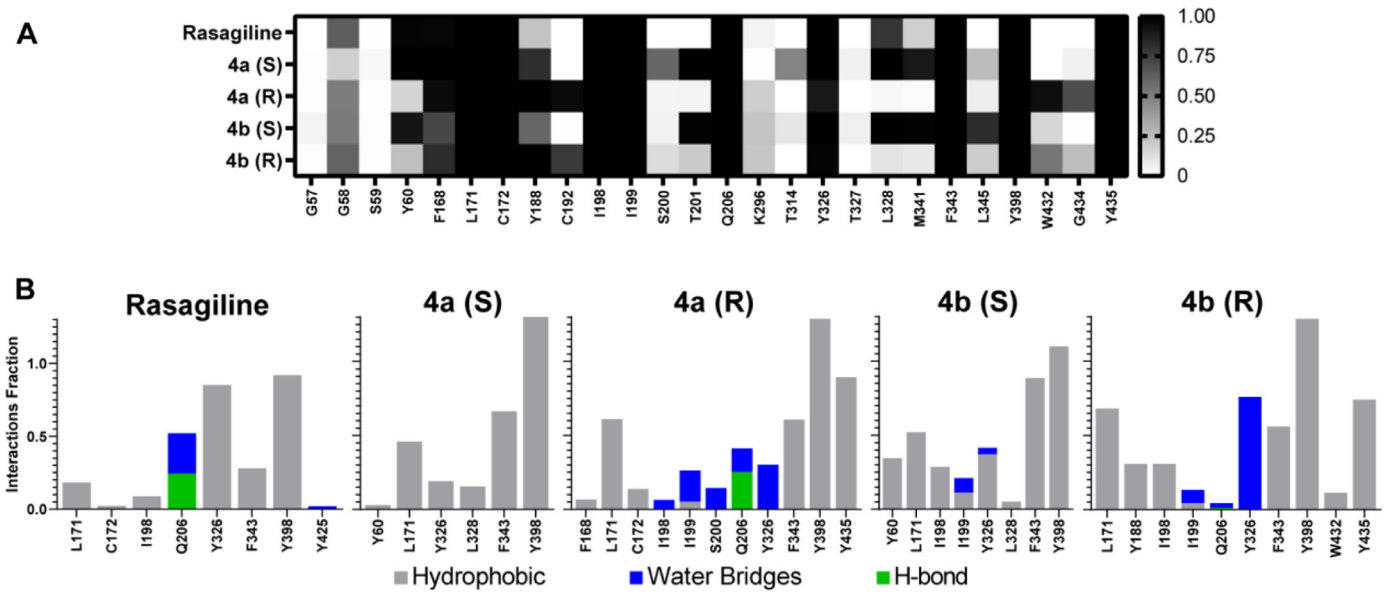

Fig. 12. A) Contact frequencies heat-map of ligands rasagiline, 4a-(*S*), 4a-(*R*), 4b-(*S*) and 4b-(*R*) with residues of the MAO-B binding site at 4 Å during the 250 ns MDs. The bar shows the frequency scale. B) Interactions between the residues of MAO-B and ligands rasagiline, 4a-(*S*), 4a-(*R*), 4b-(*S*) and 4b-(*R*), categorized into three types: hydrophobic, water bridges, and hydrogen bonds. The stacked bar charts are normalized over the course of the unrestrained 250 ns MDs.

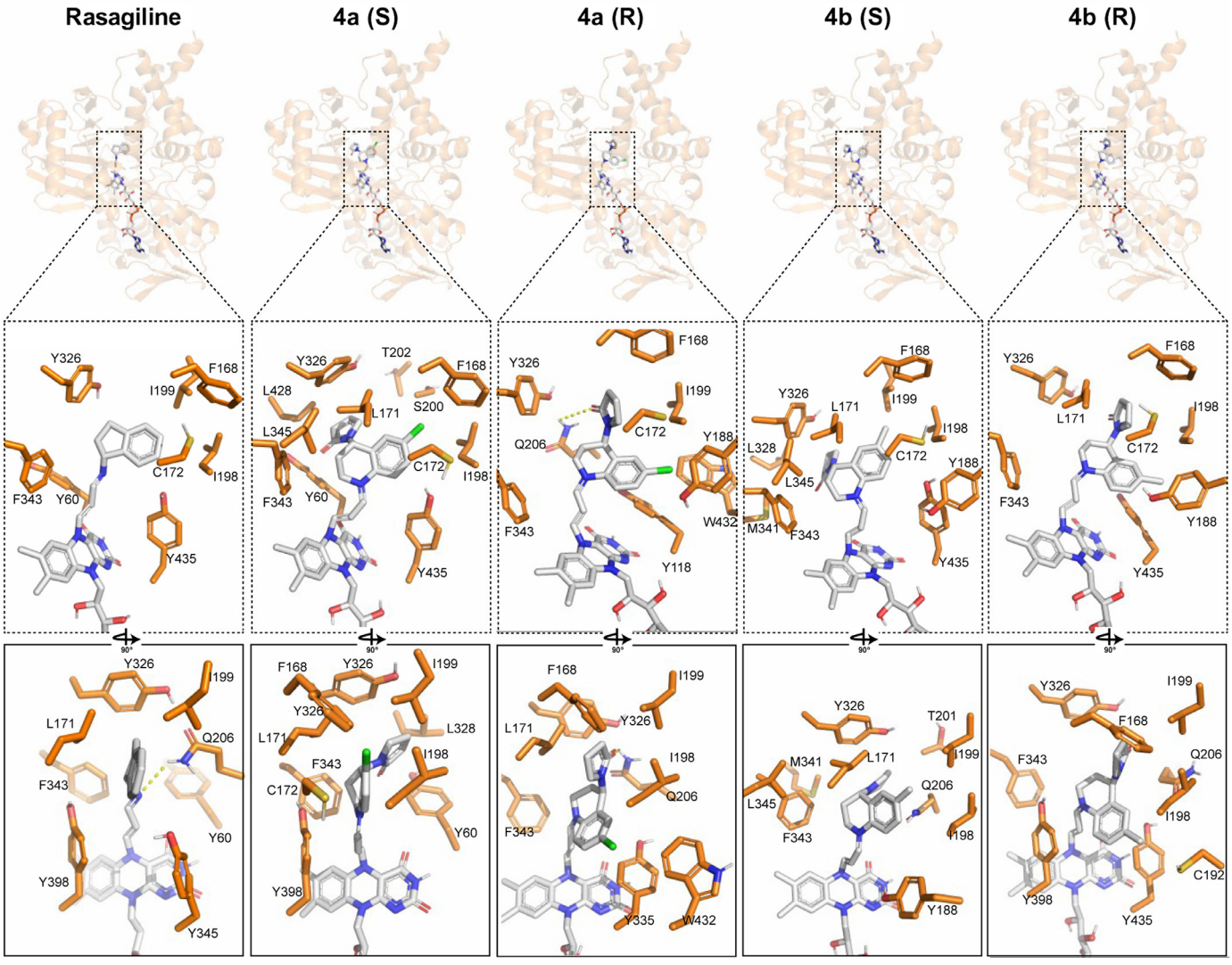

Fig. 13. Interaction site of Rasagiline, 4a-(*S*), 4a-(*R*), 4b-(*S*) and 4b-(*R*) in MAO-B.

characterized by ATR-FTIR, ^{1}H-NMR, ^{13}C-NMR spectroscopy, and ESI-MS. ATR-FTIR allowed to identify an absorption band for the propargyl fragment vibrations (3212 cm^{-1} for **4a**, and 3209 cm^{-1} for **4b**) and the carbonyl group vibration (1667 cm^{-1} for **4a**, and 1670 cm^{-1} for **4b**). ESI-MS showed an adduct $[M+Na]^{+}$ in both compounds, **4a** and **4b**, that corresponded to 291.1 and 311.1 m/z, respectively. ^{1}H-NMR spectra revealed a triplet signal at 2.14 and 2.16 ppm for **4a** and **4b**, respectively, which correspond to a hydrogen of the propargyl fragment.

4. Conclusions

The synthesis of *N*-propargylamines continues to be of interest in the development of new drugs to treat neurodegenerative disorders such as Huntington's, Parkinson's and Alzheimer's diseases [14]. The well-known MAO-B inhibitors selegiline (**1**) and rasagiline (**2**) are drugs used in the treatment of Parkinson's disease (PD) which bear an *N*-propargylamine group. Since the therapeutic effect of these drugs is related to the ability of the *N*-propargyl group to form an adduct with the FAD co-factor [17] the synthesis of new propargylamines which may target multiple neurodegenerative diseases, have neurorestorative capability, and have fewer undesirable effects is of utmost importance. In this contribution, it has been shown that the $InCl_3$ catalyzed cationic Povarov reaction is a feasible and easy route to new *N*-propargylamines. Single crystal X ray diffraction studies allowed to determine the structure of the new compounds, **4a** and **4b**, which may form adducts with the FAD cofactor. The description of their crystal structures in terms of hydrogen bonds and C-H$\cdots\pi$ interactions and the subsequent Hirshfeld surface analyses, energy frameworks and E_{xy} enrichment ratio calculations provided greater insight into factors that help stabilize the structure and that may play an important role in inhibiting MAO-B by interacting with different donors and acceptors within the MAO-B cavity. Molecular dynamics simulations indicate that **4a** and **4b** interact with groups within that cavity in a similar way as rasagiline. As reported by Tandarić and Vianello [17] the efficient binding of rasagiline (and even more efficient for selegiline) is due to hydrophobic C-H$\cdots\pi$ and $\pi\cdots\pi$ interactions with neighboring residues (active site tyrosines and FAD) and favorable N-H$\cdots\pi$ interactions. The fingerprint plots obtained in the Hirshfeld surface analysis showed that in compounds **4a** and **4b** there is a high contribution from H$\cdots\pi$(*C*g) and H$\cdots\pi$(C≡C) contacts (24.8% and 25.4%, respectively) which can account for favorable interactions. In addition, O$\cdots$H interactions, which represent 9.9% and 10.0% (**4a** and **4b**), provide opportunities for hydrogen bonding within the active site. This is consistent with the propensities to form those interactions obtained from the contact enrichment ratios. As it was discussed in Section 3.2, O$\cdots$H, C$\cdots$H, and N$\cdots$H interactions in compound **4a** and Cl$\cdots$N, O$\cdots$H, C$\cdots$H, and Cl$\cdots$H interactions in **4b** are highly favored and therefore will play an important role on the binding to MAO-B. Therefore, these and other related compounds containing aromatic substituents and groups rich in π-electrons should be explored to assess their potential as therapeutic alternatives for the treatment of neurodegenerative diseases. Several related compounds have been prepared in our laboratory and are being studied. The results of these studies will be published elsewhere.

Supplementary data

CCDC 2082183 and 2082184 contain the supplementary crystallographic data for this paper. These data can be obtained free of charge via www.ccdc.cam.ac.uk/structures (or from the Cambridge Crystallographic Data Centre, 12, Union Road, Cambridge CB2 1EZ, UK; fax: +44 1223 336033).

Declaration of Competing Interest

The authors declare that they have no known competing financial interests or personal relationships that could have appeared to influence the work reported in this paper.

CRediT authorship contribution statement

Fausto M. Güiza: Investigation, Methodology, Validation. **Yeray A. Rodríguez-Núñez:** Investigation, Methodology, Validation, Writing – original draft. **David Ramírez:** Formal analysis, Visualization, Writing – original draft. **Arnold R. Romero Bohórquez:** Conceptualization, Investigation, Methodology, Resources, Validation, Writing – original draft, Writing – review & editing, Supervision. **José Antonio Henao:** Formal analysis, Data curation, Validation. **Robert A. Toro:** Formal analysis, Validation, Visualization. **José Miguel Delgado:** Formal analysis, Validation, Visualization. **Graciela Díaz de Delgado:** Formal analysis, Methodology, Validation, Visualization, Writing – original draft, Writing – review & editing.

Acknowledgment

The authors thank *Vicerrectoría de Investigación y Extensión*, Universidad Industrial de Santander (UIS) and *Laboratorio de Rayos-X–Parque Tecnológico Guatiguará*, UIS, Piedecuesta, Santander, Colombia, for their support to the diffraction data collection facilities. We want to thank *Laboratorio de Espectrometría de Masas–Parque Tecnológico Guatiguará* for data collection. Y.A.R.N. thanks FONDECYT Post-Doctoral Fellowship No. 3190557. D.R. thanks FONDECYT grant No 11180604 and CONICYT-PCI REDES grant No 190074. Access to the Cambridge Structural Database for Universidad de Los Andes, Mérida, Venezuela, is possible through the *Frank H. Allen International Research & Education Programme* (FAIRE) from the Cambridge Crystallographic Data Centre (CCDC).

Supplementary materials

Supplementary material associated with this article can be found, in the online version, at doi:10.1016/j.molstruc.2021.132280.

References

[1] W.S. Bremner, M.G. Organ, Formation of substituted pyrroles via an imine condensation/aza-claisen rearrangement/imine−allene cyclization process by MAOS, J. Comb. Chem. 10 (1) (2008) 142–147, doi:10.1021/cc700159u.
[2] B. Alcaide, P. Almendros, J.M. Alonso, I. Fernández, G. Gómez-Campillos, M.R. Torres, A gold-catalysed imine–propargylamine cascade sequence: synthesis of 3-substituted-2,5-dimethylpyrazines and the reaction mechanism, Chem. Commun. 50 (35) (2014) 4567–4570, doi:10.1039/c4cc01485e.
[3] G. Cheng, Y. Weng, X. Yang, X. Cui, Base-promoted N-pyridylation of heteroarenes using N-propargyl enaminones as equivalents of pyridine scaffolds, Org. Lett. 17 (15) (2015) 3790–3793, doi:10.1021/acs.orglett.5b01733.
[4] A.A. Nechaev, A.A. Peshkov, K. Van Hecke, V.A. Peshkov, E.V. Van der Eycken, Synthesis of thiazolidine-2-thiones through a one-pot A3-coupling–carbon disulfide incorporation process, Eur. J. Org. Chem. 2017 (6) (2017) 1063–1069, doi:10.1002/ejoc.201601103.
[5] M. Arrowsmith, M.S. Hill, G. Kociok-Köhn, Group 2 catalysis for the atom-efficient synthesis of imidazolidine and thiazolidine derivatives, Chem. Eur. J. 21 (29) (2015) 10548–10557, doi:10.1002/chem.201501328.
[6] M. Arrowsmith, W.M.S. Shepherd, M.S. Hill, G. Kociok-Köhn, Alkaline earth catalysis for the 100% atom-efficient three component assembly of imidazolidin-2-ones, Chem. Commun. 50 (84) (2014) 12676–12679, doi:10.1039/C4CC05223D.
[7] Y. Shunsuke, F. Kosuke, K. Satoshi, Y. Tohru, Silver-catalyzed preparation of oxazolidinones from carbon dioxide and propargylic amines, Chem. Lett. 38 (8) (2009) 786–787, doi:10.1039/c4cc05223d.
[8] L.-Q. Yan, X. Cai, X. He, H. Wang, M. Xie, Y. Zuo, Y. Shang, Synthesis of 4-styrylcoumarins via $FeCl_3$-promoted cascade reactions of propargylamines with β-keto esters, Org. Biomol. Chem. 17 (16) (2019) 4005–4013, doi:10.1039/c9ob00323a.
[9] S. Dragoni, V. Porcari, M. Travagli, D. Castagnolo, M. Valoti, Antioxidant properties of propargylamine derivatives: assessment of their ability to scavenge

peroxynitrite, J. Pharm. Pharmacol. 58 (4) (2006) 561–565, doi:10.1211/jpp.58.4.0016.
[10] M.L. Schmitt, A.-T. Hauser, L. Carlino, M. Pippel, J. Schulz-Fincke, E. Metzger, D. Willmann, T. Yiu, M. Barton, R. Schüle, W. Sippl, M. Jung, Nonpeptidic propargylamines as inhibitors of lysine specific demethylase 1 (LSD1) with cellular activity, J. Med. Chem. 56 (18) (2013) 7334–7342, doi:10.1021/jm400792m.
[11] J. Louvel, J.F.S. Carvalho, Z. Yu, M. Soethoudt, E.B. Lenselink, E. Klaasse, J. Brussee, A.P. Ijzerman, Removal of human ether-à-go-go related gene (hERG) K+ channel affinity through rigidity: a case of clofilium analogues, J. Med. Chem. 56 (23) (2013) 9427–9440, doi:10.1021/jm4010434.
[12] T.T. Denton, P. Srivastava, Z. Xia, G. Chen, C.J.W. Watson, A. Wynd, P. Lazarus, Identification of the 4-position of 3-alkynyl and 3-heteroaromatic substituted pyridine methanamines as a key modification site eliciting increased potency and enhanced selectivity for cytochrome P-450 2A6 inhibition, J. Med. Chem. 61 (16) (2018) 7065–7086, doi:10.1021/acs.jmedchem.8b00084.
[13] D.P. Becker, C.I. Villamil, T.E. Barta, L.J. Bedell, T.L. Boehm, G.A. Decrescenzo, J.N. Freskos, D.P. Getman, S. Hockerman, R. Heintz, S.C. Howard, M.H. Li, J.J. McDonald, C.P. Carron, C.L. Funckes-Shippy, P.P. Mehta, G.E. Munie, C.A. Swearingen, Synthesis and structure-activity relationships of beta- and alpha-piperidine sulfone hydroxamic acid matrix metalloproteinase inhibitors with oral antitumor efficacy, J. Med. Chem. 48 (21) (2005) 6713–6730, doi:10.1021/jm0500875.
[14] F.T. Zindo, J. Joubert, S.F. Malan, Propargylamine as functional moiety in the design of multifunctional drugs for neurodegenerative disorders: MAO inhibition and beyond, Fut. Med. Chem. 7 (5) (2015) 609–629, doi:10.4155/fmc.15.12.
[15] C. Binda, F. Hubálek, M. Li, Y. Herzig, J. Sterling, D.E. Edmondson, A. Mattevi, Binding of rasagiline-related inhibitors to human monoamine oxidases: a kinetic and crystallographic analysis, J. Med. Chem. 48 (26) (2005) 8148–8154, doi:10.1021/jm0506266.
[16] J.P. Finberg, J.M. Rabey, Inhibitors of MAO-A and MAO-B in psychiatry and neurology, Front. Pharmacol. 7 (2016) 340, doi:10.3389/fphar.2016.00340.
[17] T. Tandarić, R. Vianello, Computational insight into the mechanism of the irreversible inhibition of monoamine oxidase enzymes by the antiparkinsonian propargylamine inhibitors rasagiline and selegiline, ACS Chem. Neurosci. 10 (8) (2019) 3532–3542, doi:10.1021/acschemneuro.9b00147.
[18] F.T. Zindo, S.F. Malan, S.I. Omoruyi, A.B. Enogieru, O.E. Ekpo, J. Joubert, Design, synthesis and evaluation of pentacycloundecane and hexacycloundecane propargylamine derivatives as multifunctional neuroprotective agents, Eur. J. Med. Chem. 163 (2019) 83–94, doi:10.1016/j.ejmech.2018.11.051.
[19] N. Katagiri, S. Chida, K. Abe, H. Nojima, M. Kitabatake, K. Hoshi, Y. Horiguchi, K. Taguchi, Preventative effects of 1,3-dimethyl- and 1,3-dimethyl-N-propargyl-1,2,3,4-tetrahydroisoquinoline on MPTP-induced Parkinson's disease-like symptoms in mice, Brain Res. 1321 (2010) 133–142, doi:10.1016/j.brainres.2010.01.049.
[20] M. Kitabatake, J. Nagai, K. Abe, Y. Tsuchiya, K. Ogawa, T. Yokoyama, K. Mohri, K. Taguchi, Y. Horiguchi, Facile synthesis and in vitro properties of 1-alkyl- and 1-alkyl-N-propargyl-1,2,3,4-tetrahydroisoquinoline derivatives on PC12 cells, Eur. J. Med. Chem. 44 (10) (2009) 4034–4043, doi:10.1016/j.ejmech.2009.04.035.
[21] Y.A. Rodriguez Núñez, M. Norambuena, A.R. Romero Bohorquez, A. Morales-Bayuelo, M. Gutiérrez, Efficient synthesis and antioxidant activity of novel N-propargyl tetrahydroquinoline derivatives through the cationic Povarov reaction, Heliyon 5 (8) (2019) e02174, doi:10.1016/j.heliyon.2019.e02174.
[22] Y.A. Rodríguez, M. Gutiérrez, D. Ramírez, J. Alzate-Morales, C.C. Bernal, F.M. Güiza, A.R. Romero Bohórquez, Novel N-allyl/propargyl tetrahydroquinolines: synthesis via three-component cationic imino diels–alder reaction, binding prediction, and evaluation as cholinesterase inhibitors, Chem. Biol. Drug Des. 88 (4) (2016) 498–510, doi:10.1111/cbdd.12773.
[23] C. Binda, F. Hubálek, M. Li, Y. Herzig, J. Sterling, D.E. Edmondson, A. Mattevi, Crystal structures of monoamine oxidase b in complex with four inhibitors of the N-propargylaminoindan class, J. Med. Chem. 47 (7) (2004) 1767–1774, doi:10.1021/jm031087c.
[24] Rigaku/MSC, Inc.CRYSTALCLEAR, Software Users Guide, version 1.3.6, The Woodlands, TX, USA, 2000.
[25] RigakuOxfordDiffraction*CrysAlisPro Software system*, 171.39.28e, Rigaku Corporation, Oxford, UK, 2015.
[26] G.M. Sheldrick, SHELXT - integrated space-group and crystal-structure determination, Acta Crystallogr. Sect. A, Found. Adv. 71 (1) (2015) 3–8, doi:10.1107/S2053273314026370.
[27] G.M. Sheldrick, Crystal structure refinement with SHELXL, Acta Crystallogr. Sect. C, Struct. Chem. 71 (1) (2015) 3–8, doi:10.1107/S2053229614024218.
[28] O.V. Dolomanov, L.J. Bourhis, R.J. Gildea, J.A.K. Howard, H. Puschmann, OLEX2: a complete structure solution, refinement and analysis program, J. Appl. Crystallogr. 42 (2) (2009) 339–341, doi:10.1107/S0021889808042726.
[29] K. Brandenburg, DIAMOND, Crystal Impact, GbR, Bonn, Germany, 1999.
[30] C.F. Macrae, I. Sovago, S.J. Cottrell, P.T.A. Galek, P. McCabe, E. Pidcock, et al., Mercury 4.0: from visualization to analysis, design and prediction, J. Appl. Crystallogr. 53 (1) (2020) 226–235, doi:10.1107/S1600576719014092.
[31] A.L. Spek, checkCIF validation ALERTS: what they mean and how to respond, Acta Crystallogr. Sect. E 76 (1) (2020) 1–11, doi:10.1107/S2056989019016244.
[32] F.H. Allen, O. Johnson, G.P. Shields, B.R. Smith, M. Towler, CIF applications, XV. enCIFer: a program for viewing, editing and visualizing CIFs, J. Appl. Crystallogr. 37 (2) (2004) 335–338, doi:10.1107/S0021889804003528.
[33] P.R. Spackman, M.J. Turner, J.J. McKinnon, S.K. Wolff, D.J. Grimwood, D. Jayatilaka, et al., CrystalExplorer: a program for Hirshfeld surface analysis, visualization and quantitative analysis of molecular crystals, J. Appl. Crystallogr. 54 (3) (2021) 1006–1011, doi:10.1107/S1600576721002910.
[34] M.A. Spackman, D. Jayatilaka, Hirshfeld surface analysis, Cryst. Eng. Comm. 11 (2009) 19–32, doi:10.1039/B818330A.
[35] C. Jelsch, K. Ejsmont, L. Huder, The enrichment ratio of atomic contacts in crystals, an indicator derived from the Hirshfeld surface analysis, IUCrJ 1 (2) (2014) 119–128, doi:10.1107/s2052252514003327.
[36] B. Guillot, MoProViewer: a molecule viewer for the MoPro charge-density analysis program, Acta Crystallogr. Sect. A 68 (A1) (2012) S204, doi:10.1107/S0108767312096067.
[37] Schrödinger Release 2019-1: Maestro, Schrödinger, LLC, New York, 2019.
[38] Schrödinger Release 2019-1: Desmond Molecular Dynamics System, D. E. Shaw Research, New York, 2019 Maestro-Desmond Interoperability Tools, Schrödinger, New York, 2019.
[39] K.J. Bowers, E. Chow, H. Xu, R.O. Dror, M.P. Eastwood, B.A. Gregersen, J.L. Klepeis, I. Kolossvary, M.A. Moraes, F.D. Sacerdoti, J.K. Salmon, Y. Shan, D.E. Shaw, Scalable algorithms for molecular dynamics simulations on commodity clusters, in: Proceedings of the 2006 ACM/IEEE Conference on Supercomputing, Association for Computing Machinery, Tampa, Florida, 2006 84–es, doi:10.1109/SC.2006.54.
[40] G.J. Martyna, D.J. Tobias, M.L. Klein, Constant pressure molecular dynamics algorithms, J. Chem. Phys. 101 (5) (1994) 4177–4189, doi:10.1063/1.467468.
[41] C.R. Groom, I.J. Bruno, M.P. Lightfoot, S.C. Ward, The Cambridge structural database, Acta Crystallogr. Sect. B 72 (2) (2016) 171–179, doi:10.1107/S2052520616003954.
[42] M.C. Etter, J.C. MacDonald, J. Bernstein, Graph-set analysis of hydrogen-bond patterns in organic crystals, Acta Crystallogr. Sect. B 46 (2) (1990) 256–262, doi:10.1107/S0108768189012929.
[43] J. Bernstein, R.E. Davis, L. Shimoni, N.-L. Chang, Patterns in hydrogen bonding: functionality and graph set analysis in crystals, Angew. Chem. Int. Edit. English 34 (15) (1995) 1555–1573, doi:10.1002/anie.199515551.
[44] G. Gilli, P. Gilli, in: The Nature of the Hydrogen Bond: Outline of a Comprehensive Hydrogen Bond Theory, Oxford University Press, Oxford, 2009, pp. 40–42.
[45] G. Desiraju, T. Steiner, The weak hydrogen bond, in: Structural Chemistry and Biology, Oxford University Press, Oxford, 2001, pp. 12–14.
[46] A. Afandak, H. Eslami, Ion-pairing and electrical conductivity in the ionic liquid 1-n-butyl-3-methylimidazolium methylsulfate [Bmim][MeSO4]: molecular dynamics simulation study, J. Phys. Chem. B 121 (32) (2017) 7699–7708, doi:10.1021/acs.jpcb.7b06039.